



41st European Rotorcraft Forum
1–4 September 2015, Munich, Germany
Paper 36

OPTIMISATION OF DUCTED FANS WITH CFD

Massimo Biava*, Marina Carrión*, Rene Steijl*, George N. Barakos* and David Stewart†

* CFD Laboratory, School of Engineering, University of Liverpool, L69 3GH, U.K.

† Hybrid Air Vehicles Ltd, Hangar 1, Cardington Airfield, Shortstown, Bedford, MK42 0TG, U.K.

E-mail: *M.Biava@liverpool.ac.uk*, *G.Barakos@liverpool.ac.uk*

ABSTRACT

This paper presents the performance analysis and design of a ducted propeller for lighter-than-air vehicles. High-fidelity CFD simulations were undertaken on a model with simplified geometry to quantify the effect of the duct, and to assess the influence of the blade twist on the ducted propeller performance. It is shown that the duct is particularly effective for low speed operations, and that the blades with relatively high twist have better performance over a wide range of operating conditions. Design of the optimal twist distribution was then attempted, by coupling the flow solver with a quasi-Newton optimisation method. Flow gradients were provided by a fully implicit adjoint solver for the RANS equations, which accounts for the turbulence model coupling. Results show a 2% reduction in the required power of the optimised ducted propeller. The degree of approximation introduced by the simplified geometry was also quantified, by solving the flow for a more realistic geometry and through comparison with available experimental data.

1 INTRODUCTION

Propellers are excellent in generating propulsive forces for low-speed aircraft, such as lighter-than-air vehicles (LTVs) with high efficiency. Their performance can also be augmented by enclosing them in ducts [1], that drive the expansion of their wake and increase the static pressure difference. The ducts also serve to reduce the noise emission and to protect the propeller blades. The ideal power reduction at fixed thrust due to the duct is given by momentum theory [2], and is a function of the ratio a_w between the area of the exit section of the duct and the propeller disc area. The higher the value of a_w , the higher is the power reduction. In reality, however, the value of a_w is limited by the adverse pressure gradient inside the duct diffuser, where flow separation may even take place. Therefore, the design and optimisation of the propeller duct can benefit from high-fidelity flow modelling and this target is pursued in this paper.

A baseline design of a ducted LTV propeller was provided by *Hybrid Air Vehicles Ltd* (HAV), which includes the rotor blades, the duct, and a spinner with simplified axisymmetric geometry in place of the propulsor piston engine. The performance of the baseline design (figure 1a) was studied by solving the Reynolds-Averaged Navier-Stokes (RANS) equations with the $k-\omega$ turbulence model [3] by means of the HMB2 flow solver [4, 5]. The effect of the duct was also quantified, by comparing the predicted thrust and power consumption with those of the unducted (or “free”) propeller (figure 1b). The

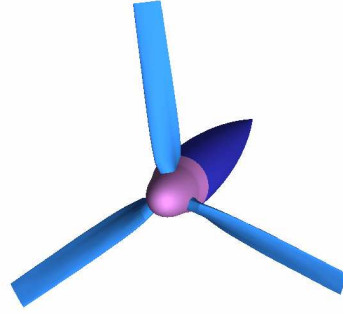
results revealed that the duct allows for an important power reduction in low speed operations, which often characterise a significant part of the typical LTV mission.

The sections and twist distribution of the baseline propulsor rotor blades are optimised without the duct, and the question is whether the design is also optimal for the ducted configuration. The present work focuses on the twist distribution and, to gain a basic understanding of the twist effect, we compared the performance of the baseline blade, that has 35° twist, with a low-twist blade, having 7° twist. The low-twist blade design was the outcome of an optimisation study for low speeds, based on a simple panel method. However, the high-fidelity CFD results indicated that the performance of the high-twist blade are superior, both at low speed (cruise speed) and at high speed (dash speed).

In light of these results, an optimisation of the blade twist distribution with CFD was attempted. The HMB2 flow solver was coupled with an external optimiser and an in-house parametrisation software for the blade surface. The computational mesh is updated at each optimisation cycle using an advanced deformation algorithm based on Inverse Distance Weighting (IDW) [6]. To minimise the expensive flow solution evaluations, a quasi-Newton optimisation method was employed. In particular, the optimiser is based on a Sequential Least-Squares Quadratic Programming (SLSQP) method [7], as provided in the software library *NLOpt* [8]. The required flow derivatives with respect to the design variables were computed using the fully implicit adjoint solver implemented in



(a) Ducted propeller.



(b) Free propeller.

Figure 1: Propulsor geometry.

HMB2 [9]. The blade with optimised twist distribution requires 2% less power with respect to the baseline design.

To keep the computational time low, the analysis of duct and twist effect and the blade twist optimisation were performed on a simplified model of the propulsor. In order to quantify the impact of the geometry simplification on the predicted performance, a more realistic model of the propulsor was also considered. It includes the nacelle enclosing the engine, the air radiators and the oil cooler. Results on the realistic model were compared to those on the simplified model, and also to available thrust and power measurements gathered during static tests. Very good agreement is observed for the realistic model results and the experiments, while results with the simplified model show a significant underestimation of the required power.

The paper is structured as follows. Section 2 describes the HMB2 base flow and adjoint solvers, and the coupling strategy with the external optimiser. Also, details about the mesh deformation algorithm are given. In section 3 the numerical results are presented. The performance of the baseline propeller is firstly analysed, for the ducted and unducted configurations. The baseline blade with high-twist is then compared with the low-twist blade design. The optimisation study with CFD follows. The optimisation method is first assessed using an aerofoil drag minimisation test case, and then applied to determine the blade optimal twist distribution for the ducted propeller. The simulations for a more realistic model of the propulsor are also presented, and results are compared to experimental measurements. Conclusions and final remarks are given in section 4.

2 NUMERICAL METHODS

2.1 The Optimisation Tool Chain

Gradient based optimisation is an efficient and widely used method for aerodynamic shape optimisation problems, since it minimises the required number of flow solutions. It requires,

however, the flow derivatives with respect to the design variables, which can be extremely expensive to compute when high fidelity CFD is employed. An economic way to obtain the flow gradients with CFD is represented by the adjoint method, which reduces the cost of flow gradients evaluation to about twice the cost of the base flow solution, regardless of the number of design variables.

The HMB2 flow solver embeds a fully implicit adjoint solver [9], which can be interfaced to any gradient based optimisation tool to solve design problems. The current implementation employs a Sequential Quadratic Programming (SQP) optimisation algorithm [7], as implemented in the software library *NLOpt* [8]. It represents the objective function as a quadratic approximation to the Lagrangian and uses a dense SQP algorithm to minimise a quadratic model of the problem. It is intended for problems with up to a few hundred constraints and variables, since the required computer memory scales with the square of the problem dimension. The SQP algorithm is implemented in a separate tool, and it is interfaced with HMB2 using files for data exchange.

The mapping between the design space and the shape to be optimised is problem specific. In aerofoil design, usually a polynomial basis, such as Chebyshev or Bernstein polynomials, is used to represent the aerofoil upper and lower surfaces. For three-dimensional objects (propeller blades, propulsor duct, etc.) more complex parametrisations might be required.

The design optimisation tool chain is described in figure 2. It can be summarised as follows.

- 1 The first step is to solve the flow around baseline geometry of the object under investigation (*e.g.* aerofoil, blade, etc.).
- 2 The cost functional I (*e.g.* drag to lift ratio, torque to thrust ratio, etc.) is evaluated from the flow solution.
- 3 The adjoint problem is solved to compute the gradient $dI/d\alpha$ of the cost functional with respect to the design variables α .

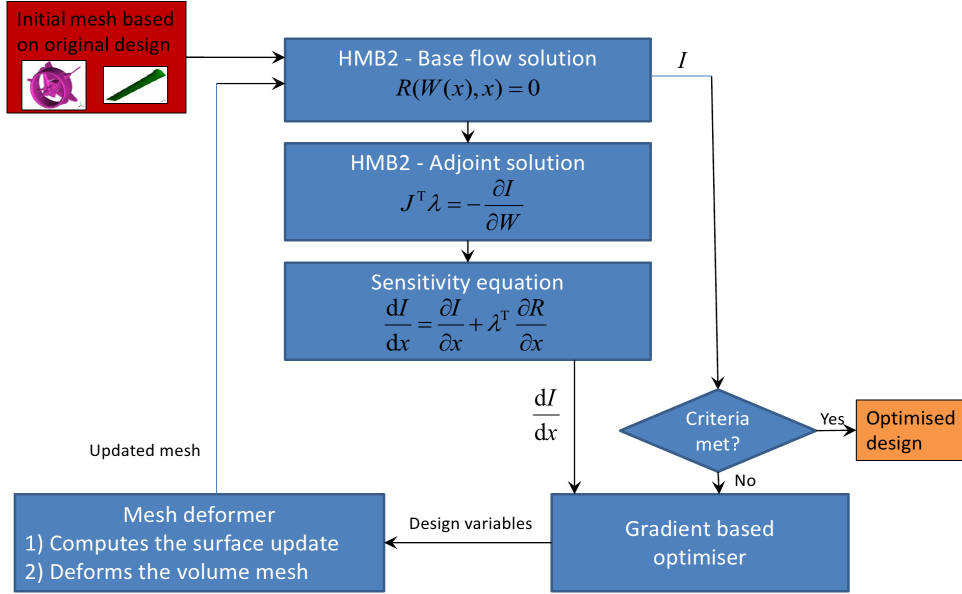


Figure 2: Flow chart of the optimisation process.

- 4 The cost functional and its gradient are fed to the gradient based optimiser, which produces a new set of design variables, corresponding to a design candidate in the search direction.
- 5 An external parametrisation software updates the object surface.
- 6 A mesh deformation algorithm computes the new volume mesh.
- 7 HMB2 solves the new flow problem and recomputes the cost functional I and its gradient $dI/d\alpha$.

Steps 2–7 are repeated for several design iterations until determined convergence criteria are met.

2.2 The Flow Solver

The following contains a brief outline of the approach used in the Helicopter Multi-Block solver version 2.0. The Navier–Stokes (NS) equations are discretised using a cell-centred finite volume approach. The computational domain is divided into a finite number of non-overlapping control-volumes V_{ijk} , and the governing equations are applied to each cell. Also, the Navier–Stokes equations are re-written in a curvilinear coordinate system which simplifies the formulation of the discretised terms since body-conforming meshes are adopted here. The spatial discretisation of the NS equations leads to a set of ordinary differential equations in real time:

$$(1) \quad \frac{d}{dt} (\mathbf{W}_{ijk} V_{ijk}) = -\mathbf{R}_{ijk}(\mathbf{W}).$$

where \mathbf{W} and \mathbf{R} are the vectors of cell conserved variables and residuals respectively. The convective terms are discretised using Osher’s upwind scheme for its robustness, accuracy, and stability properties. MUSCL variable extrapolation is used to provide second-order accuracy with the Van Albada

limiter to prevent spurious oscillations around shock waves. Boundary conditions are set using ghost cells on the exterior of the computational domain. At the far-field, ghost cells are set at the free-stream conditions. At solid boundaries the no-slip condition is set for viscous flows, or ghost values are extrapolated from the interior (ensuring the normal component of the velocity on the solid wall is zero) for Euler flow.

The integration in time of equation 1 to a steady-state solution is performed using a fully implicit time-marching scheme by:

$$(2) \quad \frac{\mathbf{W}_{ijk}^{n+1} - \mathbf{W}_{ijk}^n}{\Delta t} = -\frac{1}{V_{ijk}} \mathbf{R}_{ijk}(\mathbf{W}_{ijk}^{n+1}),$$

where $n + 1$ denotes the real time $(n + 1)\Delta t$. For steady state problems, the real time is replaced by a pseudo time (τ), that is also used for unsteady problems in the dual time stepping scheme of Jameson [10]. Equation 2 represents a system of non-linear algebraic equations and to simplify the solution procedure, the flux residual $\mathbf{R}_{ijk}(\mathbf{W}_{ijk}^{n+1})$ is linearised in time as follows:

$$(3) \quad \mathbf{R}_{ijk}(\mathbf{W}^{n+1}) \approx \mathbf{R}_{ijk}(\mathbf{W}^n) + \frac{\partial \mathbf{R}_{ijk}}{\partial \mathbf{W}_{ijk}} \Delta \mathbf{W}_{ijk},$$

where $\Delta \mathbf{W}_{ijk} = \mathbf{W}_{ijk}^{n+1} - \mathbf{W}_{ijk}^n$. Equation 2 now becomes the following linear system:

$$(4) \quad \left[\frac{V_{ijk}}{\Delta t} \mathbf{I} + \frac{\partial \mathbf{R}_{ijk}}{\partial \mathbf{W}_{ijk}} \right] \Delta \mathbf{W}_{ijk} = -\mathbf{R}_{ijk}^n(\mathbf{W}^n).$$

The left hand side of (4) is then rewritten in terms of primitive variables \mathbf{P} :

$$(5) \quad \left[\left(\frac{V_{ijk}}{\Delta t} \right) \frac{\partial \mathbf{W}_{ijk}}{\partial \mathbf{P}_{ijk}} + \frac{\partial \mathbf{R}_{ijk}}{\partial \mathbf{P}_{ijk}} \right] \Delta \mathbf{P}_{ijk} = -\mathbf{R}_{ijk}^n(\mathbf{W}^n),$$

and the resulting linear system is solved with a GCG (Generalised Conjugate Gradient) iterative solver [11]. Since at

steady state the left hand side of (5) must become zero, the Jacobian $\partial \mathbf{R} / \partial \mathbf{P}$ can be approximated by evaluating the derivatives of the residuals with a first-order scheme for the inviscid fluxes. The first-order Jacobian requires less storage and, being more dissipative, ensures a better convergence rate to the GCG iterations.

The steady state solver for the turbulent case is formulated and solved in an identical manner to that of the mean flow. The eddy-viscosity is calculated from the latest values of k and ω (for example) and is used to advance both the mean flow solution and the turbulence solution. An approximate Jacobian is used for the source term by only taking into account the contribution of the dissipation terms \hat{D}_k and \hat{D}_ω , i.e. no account of the production terms is taken on the left hand side of the system.

2.3 The Fully Implicit Adjoint Solver

An efficient way to compute the derivatives of the cost functional with respect to design variables, is via solving the *sensitivity equation* casted in adjoint form. The underlying idea is to write explicitly the cost functional I as a function of the flow variables \mathbf{W} and of the design variables α , that is, $I = I(\mathbf{W}(\alpha), \alpha)$. The flow variables are subject to satisfy the fluid dynamics governing equations (e.g. the Navier–Stokes equations) written in compact form as

$$(6) \quad \mathbf{R}(\mathbf{W}(\alpha), \alpha) = 0.$$

Formally, taking the derivative of I with respect to α we obtain:

$$(7) \quad \frac{dI}{d\alpha} = \frac{\partial I}{\partial \alpha} + \frac{\partial I}{\partial \mathbf{W}} \frac{\partial \mathbf{W}}{\partial \alpha}.$$

By introducing the adjoint variable λ as the solution of the following linear system:

$$(8) \quad \left(\frac{\partial \mathbf{R}}{\partial \mathbf{W}} \right)^T \lambda = - \left(\frac{\partial I}{\partial \mathbf{W}} \right)^T,$$

equation (7) can be rewritten as:

$$(9) \quad \frac{dI}{d\alpha} = \frac{\partial I}{\partial \alpha} + \lambda^T \frac{\partial \mathbf{R}}{\partial \alpha},$$

The computational cost of the dual sensitivity problem (8)-(9) scales with the number of outputs, since the right-hand side of (8) depends on I , but it is independent of the input parameters. The adjoint form of the sensitivity equation is therefore particularly efficient for aerodynamic optimisation applications, where usually the number of (output) cost functionals is small, while the number of (input) design variables is large.

The linear system (8) for computing the adjoint variable is solved with a fixed-point iteration scheme, where an approximation of the linear system matrix, with better condition number, is introduced as a preconditioner to advance the solution at each iteration [12, 13]. The fixed-point iterative scheme reads:

$$(10) \quad \hat{J}^T \Delta \lambda^{n+1} = - \left(\frac{\partial I}{\partial \mathbf{W}} \right)^T - J^T \lambda^n$$

where

$$J = \frac{\partial \mathbf{R}}{\partial \mathbf{W}}, \quad \hat{J} = \frac{V}{\Delta t} \mathbf{I} + \left[\frac{\partial \mathbf{R}}{\partial \mathbf{W}} \right]^{\text{1st}}, \quad \Delta \lambda^{n+1} = \lambda^{n+1} - \lambda^n.$$

The preconditioner \hat{J} is the matrix used for the base flow implicit update (5), and consists of the sum of a stabilising pseudo-time derivative term and of the first-order residual Jacobian (e.g. the Jacobian evaluated using a first-order scheme for the inviscid fluxes, and having the sparsity pattern induced by the inviscid equations stencil). The fixed point iteration (10) is solved using a GCG iterative scheme [11].

The iteration scheme (10) do not require the full exact Jacobian J , but only the matrix-vector product $J^T v$. The computer code to perform the product is obtained by automatic differentiation in reverse mode of the flow steady residual function [9]. This avoids storing J , and hence the computation of sensitivities adds only a small memory overhead to the base solver.

2.4 Mesh Deformation

To adapt the volume mesh to the surface generated by the parametrisation software at each optimisation iteration, an advanced mesh deformation algorithm has been implemented into the HMB2 solver, based on Inverse Distance Weighting (IDW) [6]. IDW is an interpolation method that calculates the values at given points with a weighted average of the values available at a set of known points. The weight assigned to the value at a known point is proportional to the inverse of the distance between the known and the given point, from which stems the name of the method.

Given N samples $\mathbf{u}_i = u(\mathbf{x}_i)$ for $i = 1, 2, \dots, N$, the interpolated value of the function u at a point \mathbf{x} using IDW is given by:

$$(11) \quad \mathbf{u}(\mathbf{x}) = \begin{cases} \frac{\sum_{i=1}^N w_i(\mathbf{x}) \mathbf{u}_i}{\sum_{i=1}^N w_i(\mathbf{x})}, & \text{if } d(\mathbf{x}, \mathbf{x}_i) \neq 0 \text{ for all } i \\ \mathbf{u}_i, & \text{if } d(\mathbf{x}, \mathbf{x}_i) = 0 \text{ for some } i \end{cases}$$

where

$$(12) \quad w_i(\mathbf{x}) = \frac{1}{d(\mathbf{x}, \mathbf{x}_i)^p}.$$

In the above equations p is any positive real number (called the *power parameter*) and $d(\mathbf{x}, \mathbf{y})$ is the Euclidean distance between \mathbf{x} and \mathbf{y} (but any other metric operator could be considered as well).

The method in its original form tends to become extremely expensive as the sample data set gets large. An alternative formulation of the Shepard's method, which is better suited for large-scale problems, has been proposed by Renka [14]. In the new formulation the interpolated value is calculated using only the k nearest neighbours within the R -sphere (k and R are given fixed parameters). The weights are slightly modified in this case:

$$(13) \quad w_i(\mathbf{x}) = \left(\frac{\max(0, R - d(\mathbf{x}, \mathbf{x}_i))}{R d(\mathbf{x}, \mathbf{x}_i)} \right)^2, \quad i = 1, 2, \dots, k.$$

If this interpolation formula is combined with a fast spatial search structure for finding the k nearest points, it yields an efficient interpolation method suitable for large-scale problems.

The modified IDW interpolation formula is used in HMB2 to implement mesh deformation in an efficient and robust way. The idea is the following: the known displacement of points belonging to solid surfaces represent the sample data, while the displacements at all other points of the volume grid are computed using formula (11) with the weights (13). A blending function is applied to the displacements, so that they smoothly tend to zero as the distance from the deforming surface approaches R .

3 NUMERICAL RESULTS

3.1 Effect of the Duct

To model the propulsor, a system of grids is used along with the sliding mesh method available in HMB2. The sliding grids allow for the front and rear part of the intake to be meshed independently of the blades or other parts of the geometry, making the parameterisation and optimisation of the propulsor easier. This allows, for instance, to compare the performance of different blades, or of the ducted and unducted propellers, without the need to remesh the complete geometry. Moreover, since the geometry is axisymmetric, only a cylindrical sector around one blade was meshed, and periodic boundary conditions were used to account for the other blades.

The flow equations were formulated in the rotating reference frame attached to the blade, in order to reduce the computation of the flow to the solution of a steady problem. This is obvious in the case of the free propeller. When considering the ducted case, the duct is rotating with the propeller angular velocity, but in the opposite sense, in the blade attached reference frame. This can be, however, accounted through the boundary conditions, by imposing this rotational velocity to the boundary faces describing the duct surface. Since the duct geometry is invariant under rotations around the propeller axis, the flow can be still modelled as steady problem in the blade reference frame.

To assess the effect of the duct, we computed the performance of the ducted and free propellers, using the blade with 35° twist. The grid for the ducted and free propellers are shown in figure 3a and 3b, respectively. The former grid has 324 blocks and 9.8 million cells, while the latter has 256 blocks and 9.3 million cells.

The flow model and the operating conditions considered for the CFD simulations are summarised in the following table.

Flow equations	RANS
Turbulence model	k - ω SST
Blade angle (β)	14.1-21.2 $^\circ$
RPM	1880
Re ($=V_{\text{tip}}c_{\text{root}}/\nu_\infty$)	$3.18 \cdot 10^6$
M_{tip}	0.70
Advance ratio (J)	0, 0.136, 0.540

In the table J denotes the advance ratio of the blade:

$$(14) \quad J = \frac{V_\infty}{nD},$$

where V_∞ is the advancing velocity, n is the propeller rotational speed in revolutions per second, and D is the propeller diameter. The advance ratio $J = 0.136$ corresponds to the airship cruise speed (20 knots), while the higher advance ratio $J = 0.54$ corresponds to the airship dash speed (80 knots).

Figures 4 and 5 show, respectively, the wake visualised using the Q -criterion (isosurface $Q = 10^{-3}$) and the surface pressure coefficient (based on the free-stream velocity) on the ducted high-twist propeller at advance ratio $J = 0.54$ and blade angle $\beta = 17.2^\circ$. The blade loading shows the importance of the outboard part of the blades with high suction produced near 60% of the blade radius. The complex swirling flow is also well-resolved with the current set of CFD grids. Figures 6 and 7 compare the flow through the ducted and unducted propellers at the same flight conditions. The differences in the flow-field are substantial and well-captured by the simulation. In particular, it is clearly shown how the rear part of the duct operates as a diffuser, decreasing the propeller wake speed and increasing the static pressure, so as to induce a positive contribution to the overall thrust.

The predicted performance of the ducted and free propellers are given in tables 1 and 2, respectively. The tables report the propeller thrust and torque in physical units, the thrust and power coefficients, and the efficiency. The thrust and power coefficients are defined as:

$$(15) \quad C_T = \frac{T}{\rho n^2 D^4}, \quad C_P = \frac{T}{\rho n^3 D^5},$$

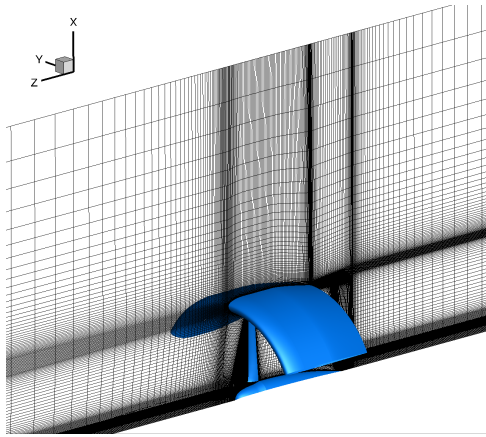
while the efficiency is given by

$$(16) \quad \eta = J \frac{C_T}{C_P}.$$

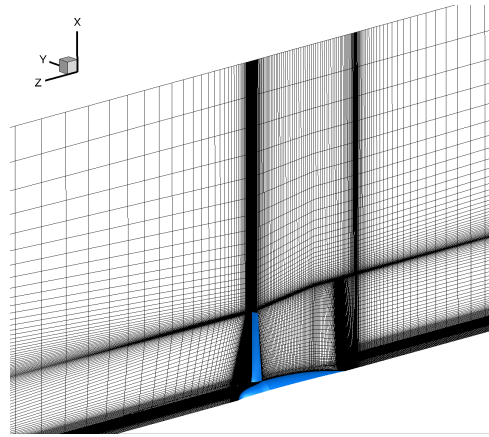
In static conditions ($J = 0$), the performance of the ducted propeller is significantly higher than that of the free propeller. For instance, with a blade angle $\beta = 14.1^\circ$ the ducted propeller gives 24% more thrust with 25% less power. At cruise speed ($J = 0.136$) the contribution of the duct is still important and, for $\beta = 17.2^\circ$ the ducted propeller gives 10% more thrust with 22% less power.

When the speed is higher, the positive effect of the duct is reduced, because the increase of its drag compensates the positive contribution of the static pressure in the diffuser. Consider, for example, the flight condition at dash speed ($J = 0.54$). At fixed angle of attack, the thrust and the torque of the ducted propeller are considerably lower, since the acceleration of the flow at the duct inlet reduces the effective angle of attack of the blade. Therefore, to compare the performance at this speed, we alter the angle of attack of the ducted propeller blades in order to match the thrust of the free propeller. Comparing tables 1 and 2, and interpolating the performance data, we deduce that the ducted propeller matches the free propeller thrust for $\beta = 20^\circ$. The torque corresponding to this blade angle is only 1% lower than the free propeller value. At this higher advance ratio the duct is ineffective on the propulsor performance.

To better understand the role of the duct in the thrust generation, we reported in tables 3–6 the force breakdown of the ducted and free propellers for cruise speed and for dash speed. At cruise speed, the duct contribution is 45% of the overall thrust, and the diffuser effect overcompensates the duct drag



(a) Ducted propeller grid.



(b) Free propeller grid.

Figure 3: Propulsor grids.

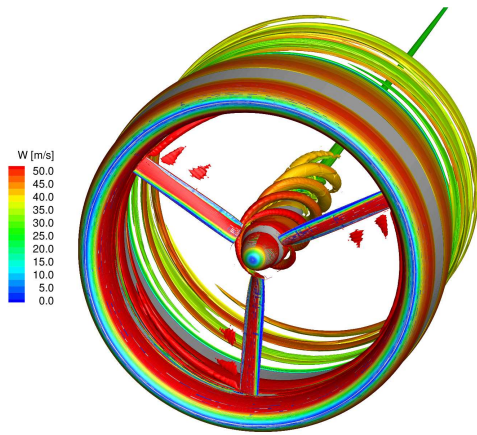


Figure 4: Visualisation of the ducted propeller wake using the Q -criterion ($J = 0.54$, $\beta = 17.2^\circ$).

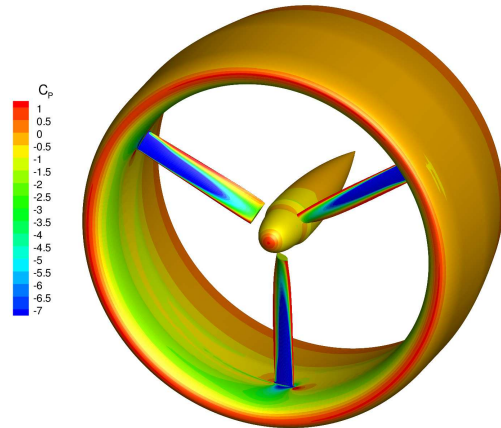


Figure 5: Distribution of the pressure coefficient on the ducted propeller ($J = 0.54$, $\beta = 17.2^\circ$).

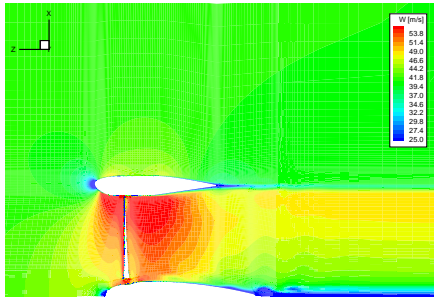


Figure 6: Distribution of the axial velocity in the vertical symmetry plane of the ducted propeller ($J = 0.54$, $\beta = 17.2^\circ$).

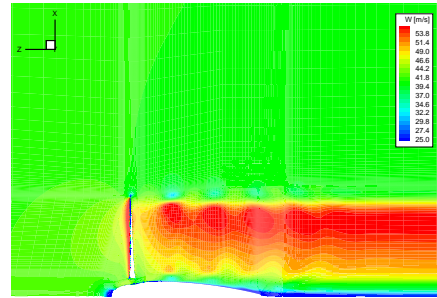


Figure 7: Distribution of the axial velocity in the vertical symmetry plane of the free propeller ($J = 0.54$, $\beta = 17.2^\circ$).

force and the reduced effective angle of attack of the propeller blades. At dash speed the contribution is reduced to 22% and it is barely sufficient to balance the negative effects. For higher speeds the duct is detrimental to the propulsor performance.

3.2 Analysis of the Twist Effect

The propulsor analysed in the previous section is equipped with rotor blades of 35° twist. Their twist distribution was designed for the free propeller, and it is therefore interesting

to verify if it is also optimal for the ducted configuration. To better understand the effect of the blade twist on the propulsor performance, and new set of blades was considered, having the same sectional shape but a lower twist value of 7° . This low-twist blade design resulted from a simplified analysis of the ducted propeller based on a panel method, aimed at maximising the performance at low speed.

The thrust and torque obtained with CFD for the ducted propeller with low-twist blades at $\beta = 17.2^\circ$ are given in table 7. The comparison with the high-twist blade results of

J	β [°]	Thrust [N]	Torque [Nm]	C_T [-]	C_P [-]	η [-]
0.000	14.1	8045	782	0.195	0.049	0.00
0.000	17.2	10197	1127	0.247	0.070	0.00
0.136	17.2	7843	1107	0.190	0.070	0.37
0.540	17.2	1970	485	0.048	0.030	0.85
0.540	19.2	3055	772	0.074	0.048	0.83
0.540	20.2	3636	934	0.088	0.059	0.81
0.540	21.2	4242	1109	0.103	0.070	0.80

Table 1: Computed performance of the ducted propeller with high-twist blade.

J	β [°]	Thrust [N]	Torque [Nm]	C_T [-]	C_P [-]	η [-]
0.000	14.1	6501	1037	0.157	0.065	0.00
0.136	17.2	7107	1381	0.172	0.087	0.27
0.540	17.2	3492	903	0.085	0.057	0.81

Table 2: Computed performance of the free propeller with high-twist blades.

Part	Thrust [N]	Torque [Nm]
Blades	4276	1073
Spinner	27	0
Duct	3540	3
Total	7843	1075

Table 3: Force breakdown on the ducted propeller ($J = 0.136$, $\beta = 17.2^\circ$).

Part	Thrust [N]	Torque [Nm]
Blades	2808	933
Spinner	39	-1
Duct	789	2
Total	3636	934

Table 5: Force breakdown on the ducted propeller ($J = 0.54$, $\beta = 20.2^\circ$).

Part	Thrust [N]	Torque [Nm]
Blades	7147	1382
Spinner	-40	0
Total	7107	1382

Table 4: Force breakdown on the free propeller ($J = 0.136$, $\beta = 17.2^\circ$).

Part	Thrust [N]	Torque [Nm]
Blades	3484	904
Spinner	8	-1
Total	3492	903

Table 6: Force breakdown on the free propeller ($J = 0.54$, $\beta = 17.2^\circ$).

J	β [°]	Thrust [N]	Torque [Nm]	C_T [-]	C_P [-]	η [-]
0.136	17.2	7841	1233	0.190	0.077	0.33
0.540	17.2	1488	457	0.036	0.029	0.68

Table 7: Computed performance of the ducted propeller with low-twist blades.

table 1 reveals that the efficiency of the low-twist blades is lower both at cruise and dash speeds. These results contradict those obtained with the simple panel method, and highlight the necessity of using high-fidelity CFD to predict accurately the performance of a ducted propeller.

The dependence of a ducted propeller performance on the blade twist was also evidenced in previous works (see, for instance, [15]), which show that an outboard bias of the blade load leads to a higher propulsive efficiency. In light of these results, an optimisation of the blade twist distribution was attempted, using a gradient based method coupled to the HMB2 flow solver. This is described in the next section.

3.3 Optimisation of the Ducted Propeller

The performance of a ducted propeller depends mainly on the blade geometry and on the expansion ratio of the duct. But

there are also other factors that might influence the performance, such as

- the shape of the duct diffuser, which needs to be designed to avoid separations due to the adverse pressure gradient;
- the shape of the duct inlet lips, whose design determines the behaviour in off-design working conditions such as, for instance, when the flow is not perfectly axial;
- the clearance between the blade tip and the duct inner surface, which affects the blade tip losses;
- the blockage induced by non-aerodynamic parts, such as purely structural component, engine, cooling devices, etc.

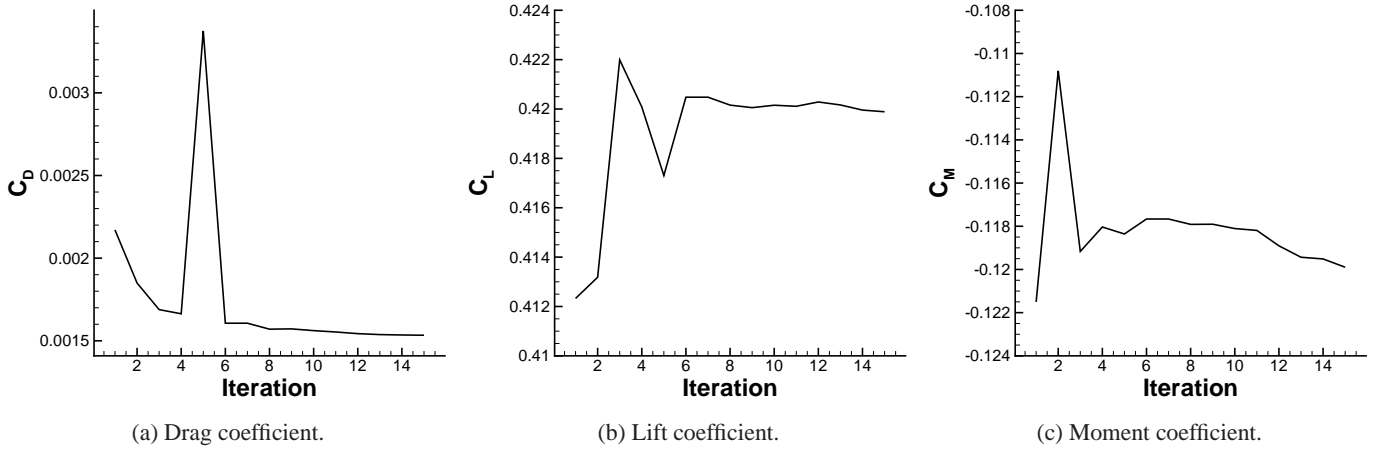


Figure 8: History of the aerofoil force coefficients during the optimisation cycles.

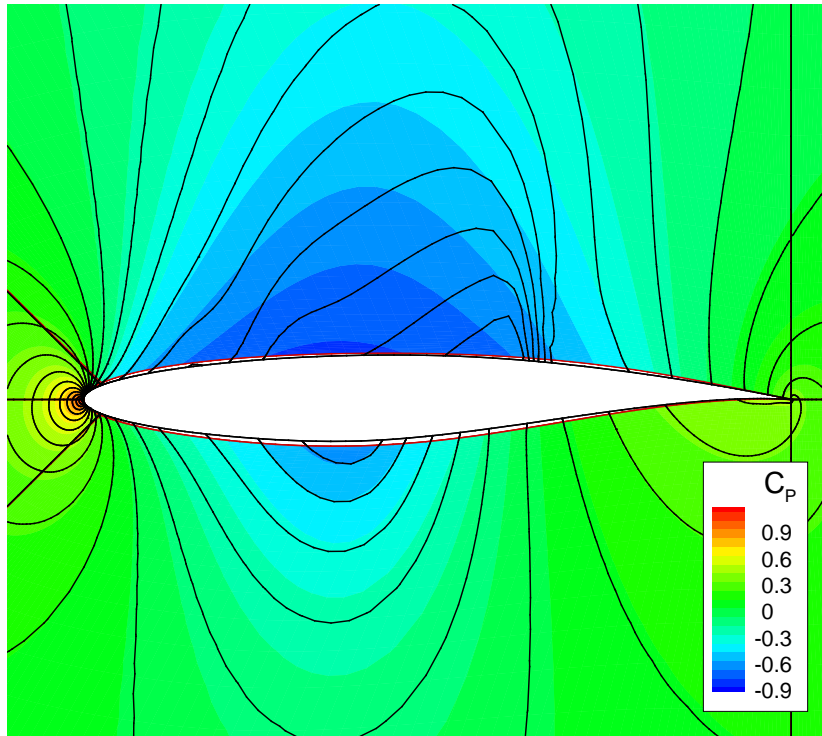


Figure 9: Comparison of the pressure coefficient distribution around the optimised aerofoil (colors) and around the original (black lines). The optimised aerofoil is drawn in red, while the baseline aerofoil is drawn in black.

In this optimisation exercise we focused on the blade geometry, in particular the blade twist distribution. However, the developed method is fairly general and shall be applied in a future work to include in the optimisation problem the duct shape and some of the listed secondary factors.

3.3.1 Assessment of the Optimisation Method

The optimisation method described in section 2 has been assessed by solving a drag minimisation problem for the RAE2822 aerofoil in transonic flight ($M = 0.75$) and zero angle of attack, with nonlinear constraints imposed on the lift, moment and thickness. The statement of the problem reads as

follows:

$$(17) \quad \begin{cases} \text{Minimise } C_D \\ \text{subject to} \\ C_L = 0.42, \\ -0.120 < C_M < -0.110, \\ t_{x=0.33} > 0.13, \end{cases}$$

where $t_{x=0.33}$ denotes the thickness of the aerofoil at 33% of the chord. The aerofoil upper and lower surfaces have been parametrised with a function of the following form (see [16]):

$$(18) \quad y(x) = C(x)S(x) + xy_{TE}, \quad x \in [0, 1],$$

where $x = 0$ and $x = 1$ are, respectively, the coordinate of the leading and of the trailing edge along the chord, and y_{TE} is

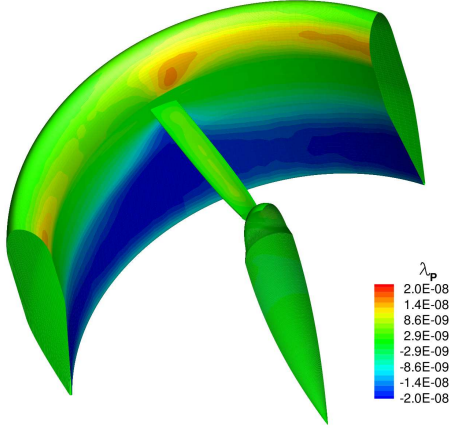


Figure 10: Pressure equation adjoint variable of the thrust coefficient C_T .

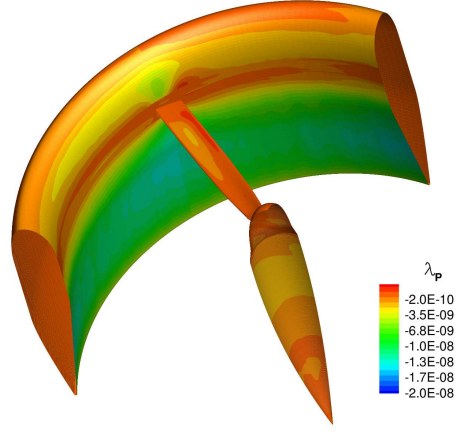


Figure 11: Pressure equation adjoint variable of the power coefficient C_P .

the y -coordinate of the trailing edge ($y_{TE} \neq 0$ only for a thick trailing edge). The term C is the so-called *class function*:

$$(19) \quad C(x) = x^{N_1}(1-x)^{N_2},$$

where $N_1 = 0.5$ and $N_2 = 1$ for an aerofoil with rounded nose and pointed aft end. The term S is instead the *shape function* and is usually represented by a polynomial. In the present work S is the sum of Bernstein polynomials of order n :

$$(20) \quad S(x) = \sum_{r=1}^n \alpha_r K_{r,n} x^r (1-x)^{n-r},$$

with

$$(21) \quad K_{r,n} = \binom{n}{r} = \frac{n!}{r!(n-r)!}.$$

The coefficient α_i , $i = 1, \dots, n$, of the polynomial expansion determine the surface shape.

To parametrise the aerofoil shape, we considered Bernstein polynomials of order 8 for the upper and lower surfaces, and a total of 16 design variables. The initial values of the polynomial expansion coefficients were determined by solving a minimisation problem to match the RAE2822 geometry. The optimisation loop converged after 15 cycles, when the cost function relative variation dropped below 10^{-3} . The history of the force coefficients is shown in figure 8. The constraint on the lift and on the moment coefficients is satisfied, and the drag is reduced by 30%. Figure 9 shows a comparison between the pressure coefficient distribution around the optimised and the original aerofoil, from which one can infer that the drag reduction is obtained by flattening the upper surface of the aerofoil, that induces a reduction of the shock strength.

3.3.2 Application to Blade Twist Optimisation

The ducted propeller with high-twist blades at the LTV cruise speed ($J = 0.136$) and blade angle of attack $\beta = 17.2^\circ$ is now considered. The baseline performance of the propulsor in these conditions are listed in table 1, from which we get

$C_T = 0.190$ and $C_P = 0.070$. The optimisation problem thus reads:

$$(22) \quad \begin{cases} \text{Minimise } C_P \\ \text{subject to} \\ C_T = 0.190. \end{cases}$$

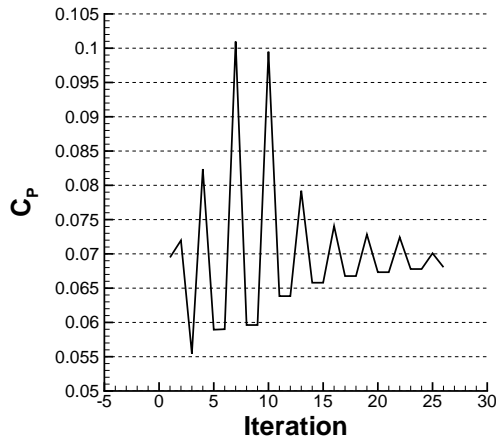
The shape of the duct is fixed, as well as the shape of the blade sections. The only permitted modification to the blade geometry is a perturbation of the initial twist distribution. This perturbation is described by a Bernstein polynomial expansion of order n :

$$(23) \quad \Delta\theta(\xi) = \sum_{r=1}^n \alpha_r K_{r,n} \xi^r (1-\xi)^{n-r},$$

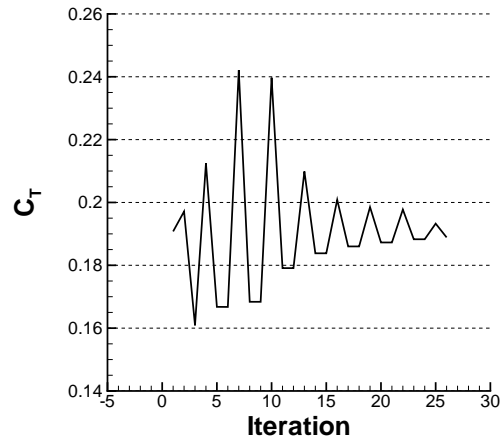
where $K_{r,n}$ is given by (21), and ξ is the blade spanwise normalised coordinate, which has value 0 in correspondence of the rotation axis and value 1 at the blade tip.

The gradients of the thrust and power coefficients with respect to the design variables α_i , $i = 1, \dots, n$, were computed using the fully implicit adjoint solver of HMB2. Figure 10 and 11 show, respectively, the distribution of the adjoint variable of the thrust and power coefficients relative to the pressure equation for the baseline design. Even if a direct interpretation of the adjoint variable is not easy, by equation (9) we can infer that modifications to surface regions with higher absolute values of the adjoint variable shall affect more the output functional (C_T or C_P). On the other hand, regions with small absolute values of the adjoint variable have negligible influence on the output functional.

We used 8 coefficients for the parametrisation (23), and each coefficient was constrained within the range $(-5^\circ, 5^\circ)$. The optimisation loop converged after 26 cycles. The history of the power and thrust coefficients during the optimisation cycles is shown in figure 12. The constraint on the thrust is satisfied within a tolerance of 10^{-3} , and the power requirement of the propulsor has been reduced by 2%. This is a modest improvement over the baseline design, and we deduce that the original 35° twist is nearly optimal for the ducted propeller configuration. Further improvement of the performance



(a) Power coefficient.



(b) Thrust coefficient.

Figure 12: History of the propulsor force coefficients during the optimisation cycles.

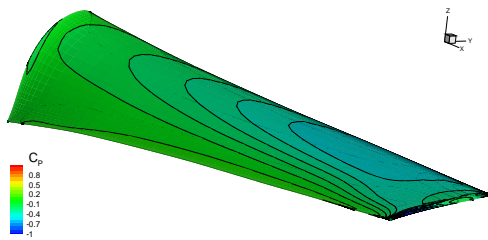


Figure 13: Pressure coefficient distribution over the baseline blade surface ($J = 0.137$, $\beta = 17.2^\circ$).

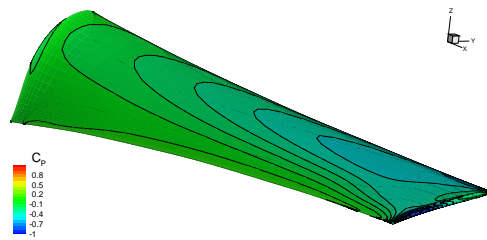


Figure 14: Pressure coefficient distribution over the optimised blade surface ($J = 0.137$, $\beta = 17.2^\circ$).

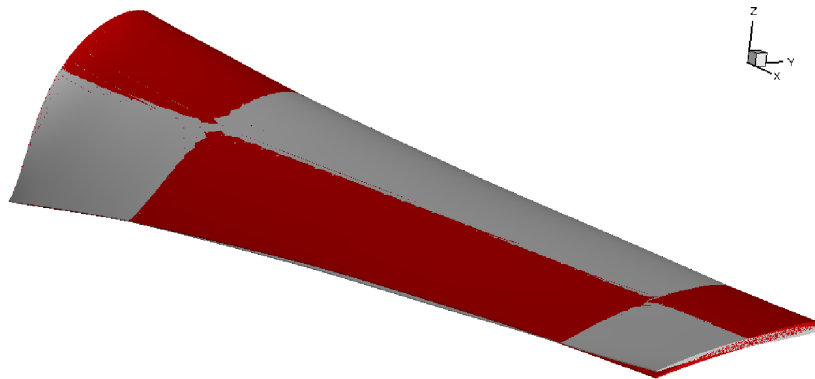


Figure 15: Comparison of baseline (gray) and optimised (red) blade surfaces.

may be achieved including the duct shape in the optimisation, which is the subject of an future work.

Figures 13 and 14 show, respectively, the pressure coefficient distributions on the baseline and the optimised blades. The latter is more loaded at the tip section and off-loaded in the mid sections. Figure 15 compares the baseline and optimised blade surfaces, and shows how the local pitch has been increased next to the blade tip and at the root, and decreased in the inner sections between 30% and 90% of the blade span.

3.4 Simulations with Realistic Geometry

The CFD simulations for the duct and blade twist assessment, and for the blade twist optimisation, were performed on a sim-

plified model of the real propulsor. To verify the degree of approximation introduced by such simplifications of the geometry, a more realistic model of the propulsor is now considered, which includes the nacelle enclosing the engine, the air radiators and the oil cooler (see figure 16).

The CFD grid for this model counts 1171 blocks and 33.5 million cells. To save computational time, the flow problem was formulated in the blade attached reference frame and modelled as a steady flow. As was done for the simplified geometry, the relative motion between the propeller and the fixed parts is completely accounted for through the boundary conditions.

The radiators and coolers were included in the CFD computations as infinitely thin walls, by setting up a solid wall



Figure 16: Ducted propeller with nacelle, radiators and cooler.

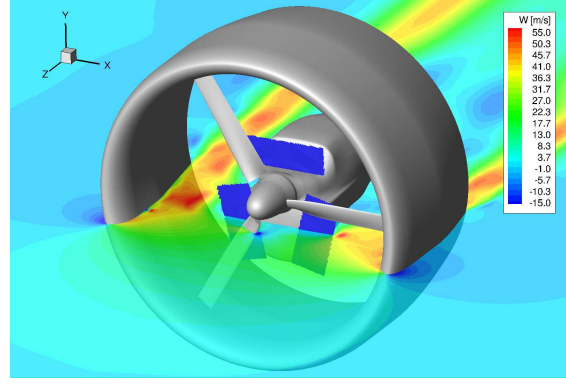


Figure 17: Distribution of the axial velocity in a horizontal plane of the ducted propeller with nacelle, radiators and cooler ($J = 0$, $\beta = 14.1^\circ$).



Figure 18: Propulsor test rig (Source *Hybrid Air Vehicles*).

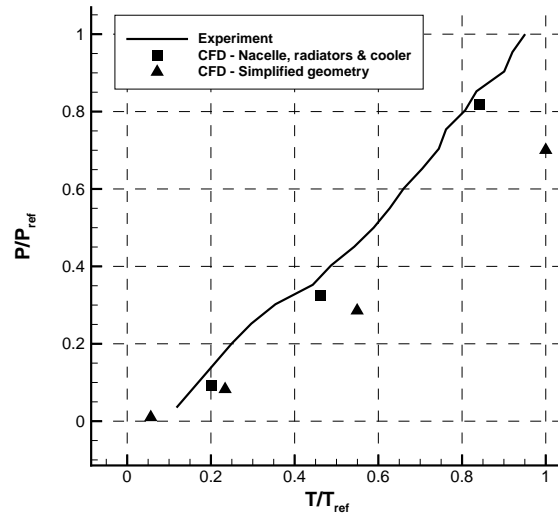


Figure 19: Comparison between predicted and measured power/thrust curve (normalised).

boundary at the interface between two adjacent grid blocks [17]. The location of these thin walls, which must have rectangular shape, is specified by giving their corner points coordinates. The flow solver HMB2 automatically localises the set of block boundary cells that approximates best the rectangular region and flags this cells as solid boundaries.

Experimental data is available from static tests of the propulsor conducted by *Hybrid Air Vehicles* on a dedicated test rig (see figure 18). The test conditions were replicated with CFD simulations using the simplified geometry of figure 1a and the more detailed model of figure 16. The flow model and the considered test conditions are listed in the following table.

Flow equations	RANS
Turbulence model	$k-\omega$ SST
Blade angle (β)	14.1°
RPM	940-1880
$Re (=V_{tip}c_{root}/\nu_\infty)$	$1.59-3.18 \cdot 10^6$
M_{tip}	0.35-0.70
Advance ratio (J)	0

The complex flow through the propulsor is shown in fig-

ure 17, that allows to appreciate the blockage introduced by the nacelle, the radiators and the cooler. The predicted performance, using both the simplified and the realistic model, are compared to the experimental measurements in figure 19. The plot reveals the importance of using a more detailed representation of the real geometry. Indeed, there is a good agreement between the CFD results for the realistic model and the experiments, while the simplified model significantly underestimates the required power. Therefore, this realistic model will be used to assess the result of the blade twist optimisation, to verify that the obtained performance improvement is valid also for the real propulsor.

4 CONCLUSIONS

This paper presented the analysis and design of a ducted propeller by means of CFD methods. The numerical results obtained with a simplified model prove the effectiveness of the duct for low speed operation, where it significantly increases the overall propulsor efficiency. The effect of the blade twist on the performance was then analysed, and results indicate that

blades with load more biased outboard operate with higher efficiency over a wide range of operating conditions. Optimisation of the twist distribution was attempted, using a quasi-Newton method and an adjoint solver to provide the required gradients. A 2% decrease in the power requirement was obtained. Simulations based on a more realistic model of the propulsor, that includes engine and cooling devices, were also performed, and results are shown to agree well with available experimental tests. Future work will consider the duct shape within the optimisation process, which is believed to potentially yield a further reduction of the power consumption. In addition, the optimised propeller performance will be verified using the realistic model.

ACKNOWLEDGMENTS

The research leading to these results has received funding from the LOCATE project of *Hybrid Air Vehicles* and *Innovate UK* (grant agreement n° 101798).

REFERENCES

- [1] B. W. McCormick. *Aerodynamics of V/STOL Flight*. Dover Publications, 1999.
- [2] J. Pereira. “Hover and Wind-Tunnel Testing of Shrouded Rotors for Improved Micro Air Vehicle Design”. PhD thesis. University of Maryland, College Park, MD, 2008.
- [3] D.C. Wilcox. “Re-Assessment of the Scale-Determining Equation for Advanced Turbulence Models”. In: *AIAA Journal* 26.11 (1988), pp. 1299–1310.
- [4] R. Steijl, G. Barakos, and K. Badcock. “A framework for CFD analysis of helicopter rotors in hover and forward flight”. In: *International journal for numerical methods in fluids* 51.8 (2006), pp. 819–847.
- [5] G. Barakos et al. “Development of CFD Capability for Full Helicopter Engineering Analysis”. In: *31st European Rotorcraft Forum*. 2005.
- [6] D. Shepard. “A Two-dimensional Interpolation Function for Irregularly-spaced Data”. In: *Proceedings of the 1968 23rd ACM National Conference*. ACM '68. New York, NY, USA: ACM, 1968, pp. 517–524.
- [7] D. Kraft. “Algorithm 733: TOMP-Fortran Modules for Optimal Control Calculations”. In: *ACM Transactions on Mathematical Software* 20.3 (1994), pp. 262–281.
- [8] S. G. Johnson. *The NLOpt Nonlinear-Optimization Package*, <http://ab-initio.mit.edu/nlopt>. Tech. rep.
- [9] M. Biava, M. Woodgate, and G. N. Barakos. “Discrete Adjoint Methods for the Computation of Rotorcraft Aerodynamic Derivatives”. In: *Proceedings of the AIAA SciTech 2015 Conference, Kissimmee, FL, USA*. AIAA 2015-1491. American Institute of Aeronautics and Astronautics Inc, 2015. DOI: 10.2514/6.2015-1491.
- [10] A. Jameson. “Time Dependent Calculations Using Multigrid with Application to Unsteady Flows past Airfoils and Wings”. In: *AIAA Paper 91-1596* (1991).
- [11] O. Axelsson. *Iterative Solution Methods*. Cambridge, MA: Cambridge University Press, 1994.
- [12] B. Christianson. “Reverse Accumulation and Implicit Functions”. In: *Optimization Methods and Software* 9.4 (1998), pp. 307–322.
- [13] M. B. Giles. “On the Iterative Solution of Adjoint Equations”. In: *Automatic Differentiation of Algorithms*. Ed. by George Corliss et al. Springer New York, 2002, pp. 145–151. ISBN: 978-1-4612-6543-6.
- [14] R. J. Renka. “Multivariate Interpolation of Large Sets of Scattered Data”. In: *ACM Trans. Math. Softw.* 14.2 (June 1988), pp. 139–148. ISSN: 0098-3500.
- [15] B. G. Jimenez and R. Singh. “Effect of Duct-Rotor Aerodynamic Interactions on Blade Design for Hover and Axial Flight”. In: *Proceedings of the AIAA SciTech 2015 Conference, Kissimmee, FL, USA*. AIAA 2015-1030. American Institute of Aeronautics and Astronautics Inc, 2015. DOI: 10.2514/6.2015-1030.
- [16] B. M. Kulfan. “Universal Parametric Geometry Representation Method”. In: *Journal of Aircraft* 45.1 (2008), pp. 142–158. DOI: 10.2514/1.29958.
- [17] M. Woodgate, V. Patrikakis, and G. N. Barakos. “Rotor Computations with Active Gurney Flaps”. In: *ERCOFTAC international symposium “Unsteady separation in fluid-structure interaction”*. Mykonos, Greece, 2013.